PAPER

# Modeling fluid injection induced microseismicity in shales



IOP Publishing Journal of Geophysics and Engineering
J. Geophys. Eng. 15 (2018) 234–248 (15pp) https://doi.org/10.1088/1742-2140/aa8a27

# Modeling fluid injection induced microseismicity in shales

**José M Carcione[1], Gilda Currenti[2], Lisa Johann[3] and Serge Shapiro[3]**

[1] Istituto Nazionale di Oceanografia e di Geofisica Sperimentale (OGS), Borgo Grotta Gigante 42c, I-34010 Sgonico, Trieste, Italy
[2] Istituto Nazionale di Geofisica e Vulcanologia (INGV)—Sezione di Catania, Catania, Italy
[3] Freie Universität Berlin, Fachrichtung Geophysik, Berlin, Germany

E-mail: jcarcione@inogs.it

Received 5 May 2017, revised 15 August 2017
Accepted for publication 4 September 2017
Published 22 January 2018


**Abstract**

Hydraulic fracturing in shales generates a cloud of seismic—tensile and shear—events that can be used to evaluate the extent of the fracturing (event clouds) and obtain the hydraulic properties of the medium, such as the degree of anisotropy and the permeability. Firstly, we investigate the suitability of novel semi-analytical reference solutions for pore pressure evolution around a well after fluid injection in anisotropic media. To do so, we use cylindrical coordinates in the presence of a formation (a layer) and spherical coordinates for a homogeneous and unbounded medium. The involved differential equations are transformed to an isotropic diffusion equation by means of pseudo-spatial coordinates obtained from the spatial variables re-scaled by the permeability components. We consider pressure-dependent permeability components, which are independent of the spatial direction. The analytical solutions are compared to numerical solutions to verify their applicability. The comparison shows that the solutions are suitable for a limited permeability range and moderate to minor pressure dependences of the permeability. Once the pressure evolution around the well has been established, we can model the microseismic events. Induced seismicity by failure due to fluid injection in a porous rock depends on the properties of the hydraulic and elastic medium and *in situ* stress conditions. Here, we define a tensile threshold pressure above which there is tensile emission, while the shear threshold is obtained by using the octahedral stress criterion and the *in situ* rock properties and conditions. Subsequently, we generate event clouds for both cases and study the spatio-temporal features. The model considers anisotropic permeability and the results are spatially re-scaled to obtain an effective isotropic medium representation. For a 3D diffusion in spherical coordinates and exponential pressure dependence of the permeability, the results differ from those of the classical diffusion equation. Use of the classical front to fit cloud events spatially, provides good results but with a re-scaled value of these components. Modeling is required to evaluate the scaling constant in real cases.

Keywords: microseismicity, hydraulic fracturing, shale gas, permeability, nonlinear diffusion

(Some figures may appear in colour only in the online journal)

## 1. Introduction

Porous media exhibit elastic and inelastic deformations. In many cases, a pressure transient analysis based on constant rock properties, particularly permeability, can lead to significant errors in parameter estimation. Porous media with relatively high pore compressibilities, for example shales, can be affected by the injection of fluids under high pressure, which may lead to permeability changes as a function of pore pressure. Wu and Pruess (2000) have shown that assuming a pressure-independent permeability may lead to large errors in the pressure profile.

A realistic approach requires the modeling of shear and tensile events. Rutqvist *et al* (2015) conducted three-dimensional coupled fluid flow and geomechanical modeling of fault activation and seismicity associated with hydraulic

 

fracturing stimulation of a shale gas reservoir, during a 3 h hydraulic fracturing stage. The results are consistent with field observations. The simulations show that shale gas hydraulic fracturing results in numerous small microseismic events, as well as aseismic deformations along with the fracture propagation. The rupture zone is clearly associated with tensile and shear failure extended to a maximum radius of about 200 m from the injection well.

Kikani and Pedrosa (1991) have taken into account the effect of a pressure-dependent permeability using an exponential dependence. They obtained an analytical solution in terms of a regular perturbation series for a radial, infinite reservoir. Their solution corresponds to a line source well with a constant discharge rate inner boundary condition in a cylindrical system. Yeung *et al* (1993) considered a simplified form of the equations used by Kikani and Pedrosa (1991) to describe spherical, cylindrical and linear flow in pressure sensitive formations. The solutions apply to a large-diameter borehole with a constant pressure boundary condition.

Here, we implement two typical cases in fluid injection. Firstly, Wu and Pruess's solution for a constant mass flow in cylindrical coordinates, and secondly Yeung *et al*'s solution for a constant injection pressure in spherical coordinates. We generalize both approaches to the anisotropic case. In fact, shales are elastically and hydraulically anisotropic and fluid-rock interaction has to be described by a nonlinear diffusion equation in an anisotropic medium as shown by Hummel and Shapiro (2013). These authors have analyzed spatio-temporal characteristics of induced seismicity recorded during a hydraulic fracturing treatment in the Barnett shale. To model the diffusion of pore-fluid pressure, they introduced a new model with a nonlinear permeability based on a pressure power law, where the pressure dependence is independent of the diffusion direction. We consider an exponential relation between pore-fluid pressure and permeability (Hummel and Müller 2009, Hummel and Shapiro 2012, Hummel 2013), which has been found to be in agreement with most experimental data (Shi and Durucan 2016). Usually, the anisotropy of hydraulic permeability is much stronger than the anisotropy of elastic properties and this approximation is implicit in the present formulation. Moreover, Wu and Pruess (2000) model anisotropy of the transport properties (permeability), although the elastic properties satisfy isotropy. In any case, the major effect is on seismic waves and here we do not compute seismograms, but just determine the emission cloud.

To analyze the effects of injection and fracturing, we consider the pressure solution in spherical coordinates and obtain tensile and shear seismic sources generated by fluid injection. Fluid injection in a borehole causes an increase of the pore pressure in the surrounding rock formation, which implies a decrease of the effective stress. In turn, such a reduction can induce micro-earthquakes in zones of weakness. Tensile and shear failure occur as a consequence of the injection and the common criterion for failure is based on a critical fluid pressure for fracturing that exceeds a given tectonic stress. The criterion to obtain the critical fluid pressures that we adopt here is based on Lal (1999). These thresholds are assumed to vary on a fractal manner based on the von-Kármán correlation function (e.g., Carcione and Gei 2009, Carcione *et al* 2015). Langenbruch and Shapiro (2014) show that the elastic heterogeneity of rocks obtained from sonic and density logs along boreholes causes significant fluctuations of fracture reactivation and opening pressures. As a result, fluctuations of principal stress magnitudes are of fractal nature. Langenbruch and Shapiro (2015) showed that stress changes in the range of $10^3$–$10^7$ Pa are capable of triggering brittle failure and associated seismicity in rocks of the Earth's crust. This result validates the concept of a nearly critical state of stress in the Earth's crust and suggests that already stress changes just above perturbations caused by tidal forces ($10^3$ Pa) are enough to trigger rupturing in the most critically stressed parts of rocks (Rothert and Shapiro 2007). Here, we consider variations of the order of 6 MPa. Correlation lengths of 0.2 m are assumed on the basis that heterogeneities are smaller than the wavelength of a seismic signal. In the case of fine layering values from tens of cm to 1 m are realistic. The evolution of the hydraulic diffusivity of the medium (temporal and spatial) can be analyzed from the envelope of events by representing the distance of the events to the injection point as a function of the emission times and from the shape and extent of the microseismic cloud.

## 2. The pressure equation

The fluid-flow model combines the equation of mass conservation and Darcy's law

$$\partial_i(\rho v_i) = -\partial_t(\phi\rho) \quad \text{and} \quad v_i = -\frac{\kappa_{(i)}}{\eta}\partial_i p, \tag{1}$$

respectively (e.g., Wu and Pruess 2000), where $p$ is the fluid pressure, $v_i$ are the flux components, $\rho$ is the fluid density, $\phi$ is the formation porosity, $\kappa_i$ are the components of the permeability tensor (in its principal system), $\eta$ is the dynamic viscosity, $\partial_i$ is the spatial derivative with respect to the variable $x_i$ and $\partial_t$ or a dot above a variable denote the time derivative. In the following, an italic subindex '*i*' denotes a spatial component and a roman subindex 'i' indicates initial state. The density and the porosity can be pressure-dependent in equation (1) and we have generalized the equation given in Wu and Pruess (2000) including anisotropy of the transport properties (permeability), although the elastic properties satisfy isotropy.

The isothermal fluid and pore compressibilities are

$$C_f = \frac{1}{\rho}\frac{\partial\rho}{\partial p} \quad \text{and} \quad C_p = \frac{1}{\phi}\frac{\partial\phi}{\partial p}, \tag{2}$$

respectively (e.g., Carcione 2014). Substituting these quantities in (1) gives

$$\dot{p} = -\frac{1}{\phi\rho C}\partial_i(\rho v_i), \quad C = C_f + C_p, \tag{3}$$

where $C$ is the total compressibility, assumed to be pressure independent in this study. For constant density, we obtain

$$\dot{p} = -\frac{1}{\phi C}\partial_i v_i. \tag{4}$$

Equation (4) can be derived from Biot's theory of poroelasticity and was used by Carcione and Gei (2009) to obtain a diffusion equation describing fluid flow under borehole conditions, where the compressibility has been modified to model uniaxial stress conditions. Its expression is

$$\phi C = \frac{\alpha - \phi}{K_s} + \frac{\phi}{K_f} + \frac{\alpha^2}{K_m + \frac{4}{3}\mu_m}, \tag{5}$$

where

$$\alpha = 1 - \frac{K_m}{K_s} \tag{6}$$

(Gutierrez and Lewis 2002, Carcione and Gei 2009), where $K_s$ is the bulk modulus of the grains, $K_f = 1/C_f$ is the fluid bulk modulus, $K_m$ is the dry-rock bulk modulus and $\mu_m$ is the dry-rock shear modulus.

Permeability varies with pressure mainly because cracks re-open when the pore pressure exceeds a given threshold. There are several expressions for the pressure dependence ranging from exponential laws (e.g., Louis 1974, Pedrosa 1986, Palmer and Mansoori 1998) to power laws (Gangi 1978, 1981).

### 2.1. Solution for radial horizontal flow

We consider a horizontal plane and invariant properties along the vertical $z$-direction i.e. the problem becomes two-dimensional. Moreover, we assume an unbounded anisotropic medium regarding transport properties (permeability), i.e. $\kappa_1 \neq \kappa_2$. Combining equations (1) and (3) and eliminating $v_i$, we obtain

$$\dot{p} = \frac{1}{\phi\rho\eta C}\partial_i(\rho\kappa_i\partial_i p), \quad i = 1, 2, \tag{7}$$

where we have assumed constant viscosity and compressibility (Wu and Pruess 2000).

Next, we assume pressure-dependent permeability components of the form

$$\kappa_i(p) = \bar{\kappa}_i f(p), \qquad f(p) = \exp[(p - p_i)/p_1], \tag{8}$$

where $p_i$ is the initial pressure and $p_1$ is a reference pressure; $p_1 \to \infty$ yields the constant diffusivity case. The quantities $\bar{\kappa}_i$ are pressure independent. This exponential relation holds for many rocks (Hummel 2013).

Let us now perform the following change of coordinates

$$x_1 = x_1'\sqrt{\frac{\bar{\kappa}_1}{\bar{\kappa}}}, \quad x_2 = x_2'\sqrt{\frac{\bar{\kappa}_2}{\bar{\kappa}}}, \qquad \bar{\kappa} = \sqrt{\bar{\kappa}_1\bar{\kappa}_2}. \tag{9}$$

Equation (7) becomes

$$\dot{p} = \frac{1}{\phi\rho\eta C}\partial_i(\rho\bar{\kappa}f(p)\partial_i p), \tag{10}$$

where we have omitted the primes for simplicity. In this new system of coordinates, we may treat the problem as isotropic and use the solution obtained by Wu and Pruess (2000). This is a mathematical simplification but the physics remains anisotropic.

We now assume that the fluid is injected at a point-like location and consider cylindrical radial coordinates $r'$. In this case, equation (10) becomes

$$\frac{1}{r}\partial_r\left[\rho(p)\frac{\bar{\kappa}}{\eta}f(p)r\partial_r p\right] = C(p)\rho(p)\phi(p)\dot{p}. \tag{11}$$

Note that any solution of the pressure equation in the physical domain should consider that

$$r' = \sqrt{\frac{\bar{\kappa}}{\bar{\kappa}_1}x_1^2 + \frac{\bar{\kappa}}{\bar{\kappa}_2}x_2^2}. \tag{12}$$

The solution of equation (11) subject to a constant injection flux $Q$ at $r_0$ is given in appendix A (equation (42)).

### 2.2. Solution in spherical coordinates

Here, we assume an unbounded transversely isotropic and homogeneous medium, i.e. $\kappa_1 = \kappa_2 \neq \kappa_3$. From equation (1), eliminating $v_i$, we obtain

$$\dot{p} = \Delta_a p, \tag{13}$$

where

$$\Delta_a = D_1(\partial_1^2 + \partial_2^2) + D_3\partial_3^2 \tag{14}$$

is a modified Laplacian differential operator and

$$D_i = \frac{N\kappa_i}{\eta}, \quad N \equiv \frac{1}{\phi C} \tag{15}$$

are the diffusivity components.

Let us perform the following change of coordinates

$$x_i' = x_i\sqrt{\frac{D_0}{D_i}}, \qquad D_0 = (D_1^2 D_3)^{1/3}, \tag{16}$$

where the primes denote the coordinates in the transformed coordinate system (Shapiro *et al* 1999, Carcione and Gei 2009), which transforms $\Delta_a$ into a pure Laplacian differential operator $\Delta'$. Using (16), equation (13) becomes

$$\dot{p} = D_0\Delta' p, \tag{17}$$

where

$$\Delta' = \partial_{1'}^2 + \partial_{2'}^2 + \partial_{3'}^2. \tag{18}$$

In this new system of coordinates, we may treat the problem as isotropic. This is a mathematical simplification but the physics remains anisotropic. Any solution of the pressure equation in the physical domain should consider that

$$r' = \sqrt{\frac{D_0}{D_1}(x_1^2 + x_2^2) + \frac{D_0}{D_3}x_3^2}. \tag{19}$$

We now assume that the fluid is injected at a point-like location and consider spherical radial coordinates $r'$. In this case, equation (17) becomes

$$\dot{p} = \frac{1}{r^2}\partial_r(D_0 r^2 \partial_r p), \tag{20}$$

where we have omitted the primes for simplicity.

Next, we generalize (20) to a nonlinear pressure equation in the sense that the permeability depends on the pressure field, meaning that also the diffusivity varies with pressure. Such a nonlinear pressure equation can be expressed as

$$\dot{p} = \frac{1}{r^2}\partial_r[D(p) r^2 \partial_r p]. \tag{21}$$

In summary, we are assuming that the nonlinear behavior is exactly the same along various principal directions of the diffusivity tensor. This model was first proposed and its applicability demonstrated for a Barnett shale case study by Hummel and Shapiro (2013) (see also section 4.3 of Shapiro 2015).

The following diffusivity–pressure relation is given in Louis (1974) and Pedrosa (1986),

$$D(p) = D_0 \exp[(p - p_i)/p_1] \tag{22}$$

(see equation (8)). Usually, observed data shows an exponential dependence of permeability on effective pressure. This dependence holds for sandstones (David *et al* 1994) and even shales (Best and Katsube 1995). Recently, Shi and Durucan (2016) have shown that the exponential and nearly exponential dependences closely describe the behavior of permeability in many rocks. There is a detailed discussion of permeability laws in Shapiro (2015) (section 2.9, pp 114–116).

The flow is represented by a step function of magnitude $p_0$ at a given radius $r_0$ away from borehole. Then, the following boundary conditions hold, i.e.

$$p(r_0, t) = p_0, \quad p(r, 0) = p_i, \quad p(r \to \infty, t) = p_i. \tag{23}$$

This is equivalent to an injection pressure source. The solution of equation (21) subject to the nonlinear diffusivity (22) and boundary condition (23) is given in appendix B, equation (54). It is also given a solution for the injection flux rate at $r_0$ (equation (60)).

On the basis of the pressure dependence (22), the diffusivity components in the principal system are given by

$$D_1 \exp[(p - p_i)/p_1] \quad \text{and} \quad D_3 \exp[(p - p_i)/p_1]. \tag{24}$$

On the other hand, Gangi and Carlson (1996) have shown that another suitable power law is

$$D(p) = D_0 \left(\frac{p - p_i}{p_1}\right)^n, \tag{25}$$

where $n$ is a nonlinear exponent. $D$ becomes the classical diffusivity $D_0$ for $n = 0$. Hummel and Shapiro (2012) use basically this model, where the factor $p_1^n$ has been combined with the diffusivity $D_0$ into a single parameter that can be computed by fitting real data. The power law is predicted by the asperity model introduced by Gangi (1978) (Carcione 2014, section 7.4). However, Shi and Durucan (2016) show that Gangi's power law equations for both intact and fractured rock can be approximated, over the range of effective stresses of practical interest (10–50 MPa), by exponential equations. The characteristics of the diffusion field and the triggering front are analyzed in appendix C.

## 3. The failure criteria for tensile and shear seismic sources

Induced seismicity by failure due to fluid injection in a porous rock depends on the properties of the medium and the *in situ* stress conditions. Fluid injection creates both tensile and shear failures. By convention, stress and pressure have the same sign in the following. Let us define the three principal effective stress components as

$$\sigma_i = s_i - p, \tag{26}$$

where $s_i$ denote the total stress components. For instance, the confining (vertical) pressure is $s_3$ and the two horizontal *in situ* stresses are $s_1$ and $s_2$. Tensile failure depends on the critical tensile pressure $P_T$ and occurs when

$$\min(\sigma_i) - P_T \leqslant 0. \tag{27}$$

On the other hand, shear failure can be modeled by the octahedral stress (Drucker–Prager) criterion (e.g., Lal 1999, Colmenares and Zoback 2002). Defining the effective mean and octahedral stresses as

$$\bar{\sigma} = \frac{1}{3}(\sigma_1 + \sigma_2 + \sigma_3) \quad \text{and}$$
$$\tau = \frac{1}{3}\sqrt{(\sigma_1 - \sigma_2)^2 + (\sigma_1 - \sigma_3)^2 + (\sigma_2 - \sigma_3)^2} \tag{28}$$

respectively, the shear failure criterion is

$$\tau - \frac{\sqrt{8}}{3 - \sin\theta}(\bar{\sigma}\sin\theta + c\cos\theta) \geqslant 0 \tag{29}$$

(Lal 1999), where

$$\tan\theta \equiv \mu \tag{30}$$

is the internal friction coefficient and $c$ is the cohesive strength. The parameters $\theta$ and $c$ can be measured by triaxial tests at different hydrostatic confining stresses under the application of an axial load until failure. More realistic is the determination of these parameters from well logs, as for instance sonic logs, since compaction is the key factor. Lal (1999) proposes

$$\sin\theta = \frac{v_P - 1}{v_P + 1} \quad \text{and} \quad c = \frac{5(v_P - 1)}{\sqrt{v_P}} = 10\tan\theta, \tag{31}$$

where $v_P$ is the $P$-wave velocity given in km s$^{-1}$ and $c$ is given in MPa.

The Drucker–Prager criterion represents a smoothed version of the Mohr–Coulomb frictional failure criterion. Lal (1999) discusses the determination of the parameters and concludes that it is desirable to obtain them from wire-line data. In fact, his figure 3 plots the velocity based strength estimates, computed from both laboratory measured and sonic log-derived velocities (reported for different core depths in

the North Sea), along with the measured strength data. Both dynamic estimates are fairly good, which demonstrates that this correlation is applicable with sonic log-derived velocities. The sonic correlation is also found to be fairly satisfactory for formations other than shale.

Shear failure occurs under certain *in situ* conditions, where shear stress can develop to induce it. If the state of stress is isotropic, i.e. if $\sigma_1 = \sigma_2 = \sigma_3$, failure does not occur since the octahedral stress is zero for any value of the pore pressure. Let us assume isotropic stress on a horizontal plane, i.e, $s_1 = s_2 = \gamma s_3$, with $\gamma \leqslant 1$, meaning that the horizontal stresses are usually smaller than the vertical (lithostatic) stress (Engelder 1993). Then, the tensile criterion (27) is

$$\sigma_1 - P_T = \gamma s_3 - p - P_T \leqslant 0. \tag{32}$$

Consider now the shear failure. Let us define

$$A = \frac{\sqrt{8}\,\sin\theta}{3 - \sin\theta}, \quad B = \frac{\sqrt{8}\,c\cos\theta}{3 - \sin\theta} = 10A,$$

where we have used equation (31). Condition (29) becomes

$$s_3[\sqrt{2}\,(1 - \gamma) - A(2\gamma + 1)] + 9Ap - 30A \geqslant 0. \tag{33}$$

There is a failure pressure $p = P_S$, such that the equal sign holds in equation (33):

$$P_S = \frac{10}{3} - \frac{s_3}{9A}[\sqrt{2}\,(1 - \gamma) - A(2\gamma + 1)], \tag{34}$$

in MPa. Octahedral stress criteria has been used in Carcione *et al* (2006) and Carcione and Poletto (2013) to describe salt viscoelasticity and the brittle-ductile transition, respectively.

Here, we assume that $P_S < P_T < p_0$, so that the injection pressure is high enough to generate seismic emission. This may not occur always, since we assume a fractal behavior of the thresholds $P_S$ and $P_T$ around an average value. Then, we apply the procedure described in appendix D. The approach is similar to that of Rothert and Shapiro (2003), where these authors consider a single threshold.

## 4. Results

Finite-element numerical solutions are obtained by solving the equation of mass conservation and Darcy's law using the commercial software Comsol Multiphysics (Comsol 2014). Exploiting the symmetry of the domain, the model is designed in an axis-symmetric formulation using a quarter of a circular ring with an internal radius of $r_0 = 0.5$ m and an external radius of 2000 m. The domain is discretized in the radial direction by a set of logarithmically spaced nodes with a resolution of 0.2 m near the internal radius and increasing to 70 m at the external boundary. This discretization leads to about 21800 iso-parametric and arbitrarily distorted triangular elements connected by 44155 nodes. The choice of second-order shape functions assures a good numerical accuracy.

First, we compare the radial flow analytical solution for a constant mass injection at the wall of the borehole (see appendix A) to the numerical results. A constant pressure $p_i$ of 10 MPa is applied at the external boundary, after having verified that the boundary is far enough to not affect the numerical solution. The hydraulic diffusivity is represented by an anisotropic diagonal tensor, whose elements are pressure-dependent, following equation (22). The model is highly nonlinear due to the permeability pressure exponential law. We consider the properties given in table 1, with $p_1 = 5.5$ MPa. Wu and Pruess (2000) developed two solutions, namely their set of equations (25), (30) and equations (28), (31) (appendix A), which provide different accuracy. Their performance can be seen in figure 1, which shows the comparison for sandstone and shale at different injection times corresponding to the $x$- and $y$-directions, as indicated in the caption. As can be seen, the analytical solution is not suitable to describe pressure diffusion in shales. In contrast, increasing the permeability to values realistic for sandstones, i.e. $\kappa_1 = 0.2$ darcy and $\kappa_2 = 0.4$ darcy, the match improves. From this we conclude that Wu and Pruess's solution is only applicable for high-permeability cases. However, in this particular case, the pressure build-up is very small due to the fast fluid diffusion. The best fit for the exponential case is obtained with the set of equations (28), (31) of Wu and Pruess (2000).

**Table 1.** Medium properties, dimensions and conditions.

| | | | |
|---|---|---|---|
| $\phi$ | 0.14 | $Q$ | 0.1 kg s$^{-1}$ |
| $K_s$ | 40 GPa | $h$ | 100 m |
| $K_m$ | 20 GPa | $r_0$ | 0.5 m |
| $\mu_m$ | 15 GPa | $p_0$ | 20 MPa |
| $\kappa_1$ | 2 $\mu$darcy | $p_i$ | 10 MPa |
| $\kappa_2$ | 4 $\mu$darcy | $t_{\max}$ | 48 h |
| $\kappa_3$ | 0.5 $\mu$darcy | | |
| $K_f$ | 2.3 GPa | | |
| $\eta$ | 0.001 Pa s | | |
| $\rho_{\rm i}$ | 1000 kg m$^{-3}$ | | |

Note. Hummel (2013); Hummel and Shapiro (2013).

To verify how the analytical solutions are affected by the permeability, we calculated the misfit between the analytical and the numerical solutions for increasing permeability values by measuring the normalized root mean square error (RMSE), defined as:

$$\mathrm{RMSE} = \sqrt{\frac{\sum_k (p_k^{\rm an} - p_k^{\rm num})^2}{\sum_k (p_k^{\rm an})^2}}. \tag{35}$$

The RMSE is computed for different $\kappa_1$ (from 0.2 darcy to 2 $\mu$darcy) and $\kappa_2$ (from 0.4 darcy to 4 $\mu$darcy) (see figure 2). The misfit significantly increases with decreasing permeability.

Subsequently, we consider the solution in spherical coordinates, corresponding to a constant pressure injection:

$$\hat{p} = -\hat{p}_1 \ln\left[1 - \frac{[1 - \exp(-1/\hat{p}_1)]}{\hat{r}}\,\mathrm{erfc}\left(\frac{\hat{r} - 1}{2\sqrt{\hat{t}}}\right)\right] \tag{36}$$

(equation (55) in appendix B). The pressure and permeability profiles as a function of the spherical radial distance from the well are shown in figure 3 (in this case $p_1 = 1.5$ MPa). Due to

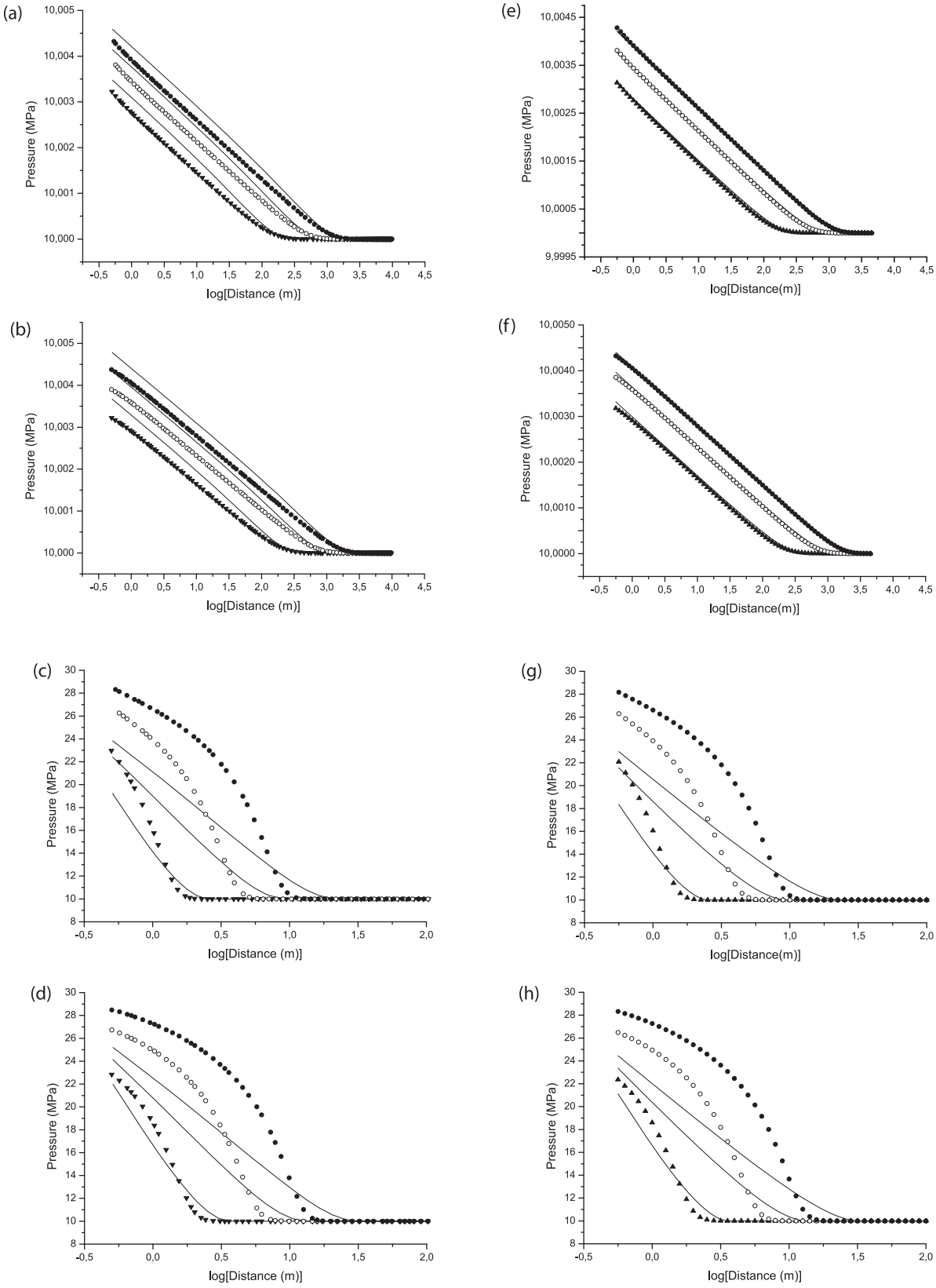


**Figure 1.** Pressure profile evolution along the $x$-direction (a), (e), (c) and (g) and $y$-direction (b), (f), (d) and (h) as a function of the radial distance from the well. The top four panels correspond to sandstone ($\kappa_1 = 0.2$ darcy and $\kappa_2 = 0.4$ darcy), while the four panels at the bottom correspond to shale, whose permeability components are those of table 1. The analytical solutions of the left and right panels are obtained with equations (25), (30) and equations (28), (31) of Wu and Pruess (2000), respectively, the latter corresponding to our equations (42), (43). The solutions correspond to cylindrical flow with a constant mass injection rate at 1 h (triangles ), 10 h (open circles) and 48 h (full circles). The solid lines refer to the analytical solution (pressure increases from left to right) and the symbols are computations obtained with Comsol.

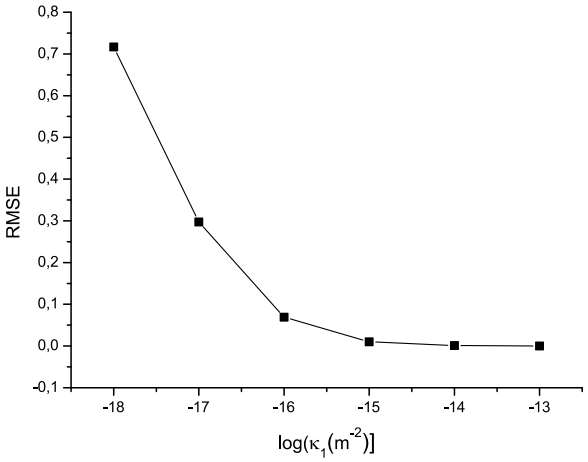


**Figure 2.** RMSE between the analytical and numerical solutions for different permeability values, corresponding to the cylindrical flow solution.

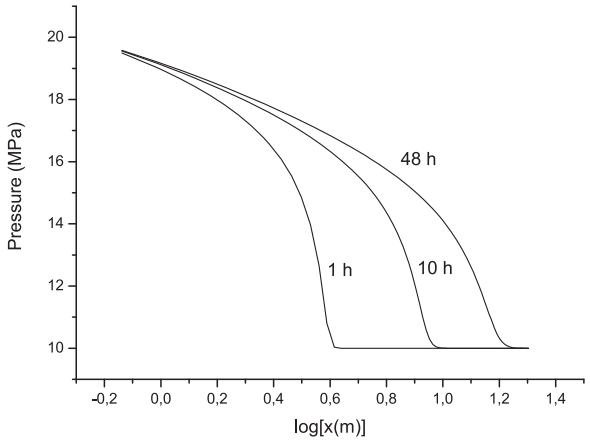


**Figure 4.** Pressure profile evolution along the $x$-direction as a function of the radial distance from the well. The solution correspond to spherical flow with a constant pressure injection at 48, 10 and 1 h (obtained with Comsol, $p_1 = 1.5$ MPa).

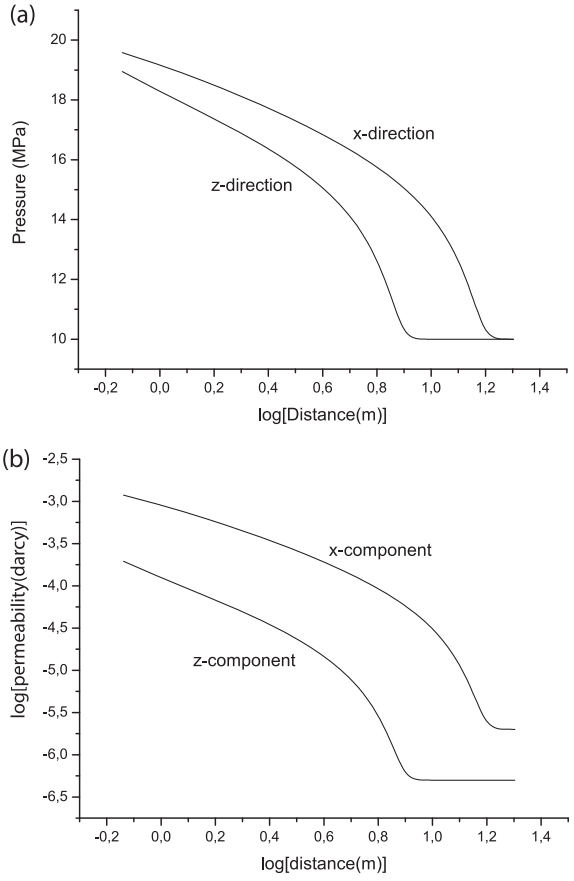


**Figure 3.** Pressure (a) and permeability (b) as a function of the spherical radial distance from the well. The solution correspond to spherical flow at 48 h with a constant pressure injection (obtained with Comsol, $p_1 = 1.5$ MPa). Due to the functional dependence with pressure (see equations (24) and (36)), the logarithm of the permeability follows qualitatively the pressure curve.

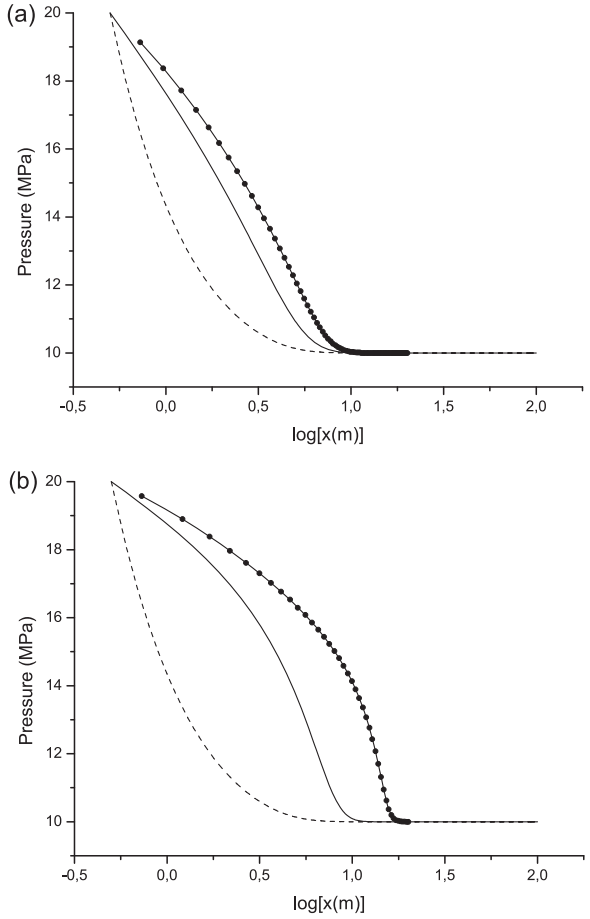


**Figure 5.** Pressure field at 48 h along the $x$-direction corresponding to spherical flow: (a) $p_1 = 3$ MPa; (b) $p_1 = 1.5$ MPa. The solid and dashed lines refer to the analytical solutions with pressure-dependent and pressure-independent permeability (equations (55) and (56)), respectively. The symbols correspond to the numerical solution obtained with Comsol.

the functional dependence with pressure (see equations (24) and (36)), the logarithm of the permeability follows qualitatively the pressure curve. As can be seen, variations in pore pressure of less than 1 MPa induce variations in permeability of one order of magnitude. The pressure evolution along the $x$-direction as a function of the distance from the well is displayed in figure 4, while figure 5 shows the pressure field at 48 h for (a) $p_1 = 3$ MPa and (b) $p_1 = 1.5$ MPa. The solid

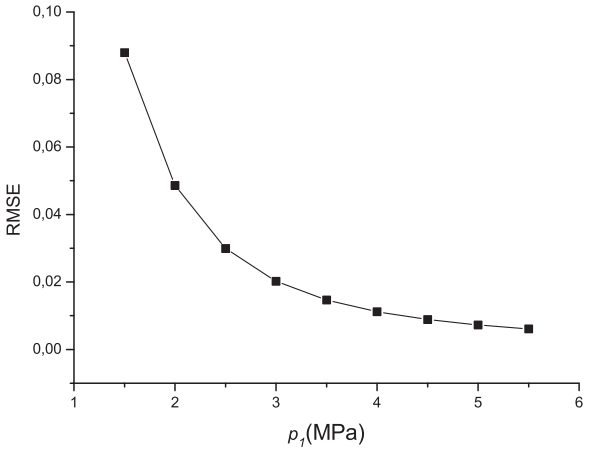


**Figure 6.** RMSE between analytical and numerical solutions for different $p_1$ values, corresponding to the spherical flow solution.

and dashed lines refer to the analytical solutions and the symbols correspond to the numerical solution obtained with Comsol. It is shown that Yeung *et al*'s approximation cannot be used when there is a strong nonlinearity as it is the case in (b). We have performed additional simulations to show how the nonlinearity affects the accuracy of the analytical solutions. Comparing the analytical and numerical solutions in the isotropic case ($\kappa_1 = \kappa_3 = 2$ $\mu$darcy), it is clear that the misfit among the solutions increases as the nonlinearity becomes higher (see figure 6). The RMSE is computed for different $p_1$ values from 1.5 to 5.5 MPa with a step of 0.5 MPa. It is worth noting that the misfit significantly increases with decreasing $p_1$. This is a consequence of failure to comply the condition $\exp[(p - p_i)/p_1] \approx 1$, for which the analytical solutions is accurate.

Let us now obtain the threshold values for the generation of tensile and shear events in order to generate seismic waves. With the properties given in table 1 ($p_1 = 5.5$ MPa), and assuming $\rho_s = 2650\,\mathrm{kg\,m^{-3}}$, $\rho_f = 1000\ \mathrm{kg\,m^{-3}}$, we obtain $v_P = 2.9\ \mathrm{km\,s^{-1}}$ from Gassmann equation ($K_G = K_m + \alpha^2 M$, $\alpha = 1 - K_m/K_s$ and $v_P = \sqrt{(K_G + 4\mu_m/3)/\rho}$, where $\rho = (1 - \phi)\rho_s + \phi\rho_f$). In the following, we assume $p_0 = 20$ MPa, $P_T = 15$ MPa (e.g., Wu 2006), $\gamma = 0.9$, $v_P = 2.9\ \mathrm{km\,s^{-1}}$ and $s_3 = 38$ MPa. We obtain $\mu = 0.56$, $\theta = 29^o$, $A = 0.55$, $B = 5.48$ MPa and $c = 5.57$ MPa. According to equation (33), the equal sign is obtained for $p = P_S = 14$ MPa. For pore pressures above this value, shear failure occurs.

Figure 7 shows a vertical section of the fractal distribution of $P_T$, where the medium has $165 \times 165$ cells with a grid spacing of $40\,\mathrm{m}/165 = 0.24\,\mathrm{m}$ along the horizontal and vertical directions. The fractal parameters are $P_0 = P_T$ ($P_0 = P_S$ in the shear case), with $\Delta P_m = 60\%\ P_0$, $\nu = 0.18$, $l = 0.2$ m and $d = 3$. If $P_T$ or $P_S$ are smaller than or equal to 10.1 MPa (slightly above $p_i$), we set their value to 10.1 MPa, since at hydrostatic values of the pore pressure we assume no seismic emission. In order to obtain the seismic emission cloud, we have to compute the pressure field around the well. This field and the threshold values computed above determine the emission points as stated in the previous section. The pressure field for $p_1 = 1.5$ MPa obtained with the Comsol software is represented in figure 8 in 3D, where the anisotropic character of the diffusion becomes clear. The field diffuses faster into the formation along the $x$-direction, since the permeability is higher than that of the vertical $z$-direction.

Figure 9 shows the tensile (a) and shear (b) emission sources after 48 h of injection, where the number of induced events is 2255 and 3081, respectively, (based on equation (48)), the scaled radius $r_0'$ at the borehole radius $r_0$ for a given event location $(x, z)$ is given by $r_0' = r_0\sqrt{(D_0/D_1)\cos^2\alpha + (D_0/D_3)\sin^2\alpha}$, where $\alpha = \tan(z/x)$. The outer front in figure 9 is a fit with equation (64),

$$\frac{|\mathbf{r}' - \mathbf{r}_0'|}{\sqrt{D_0}} \approx \sqrt{\frac{x_1^2 + x_2^2}{D_1} + \frac{x_3^2}{D_3}} = \sqrt{2t\xi} = \sqrt{6t}, \qquad (37)$$

assuming $D_1 = 2.1 \times 10^{-4}\ \mathrm{m^2\,s^{-1}}$ and $D_3 = 5.2 \times 10^{-5}\ \mathrm{m^2\,s^{-1}}$ (8 times the actual values), while the inner front (solid line) corresponds to the actual values of the (initial, at $p = p_i$) diffusivity components, i.e. $D_1 = 2.6 \times 10^{-5}\ \mathrm{m^2\,s^{-1}}$ and $D_3 = 6.6 \times 10^{-6}\ \mathrm{m^2\,s^{-1}}$ ($\xi$ is the space dimension). This discrepancy is expected since equation (37) is the diffusion front based on pressure-independent diffusivity components. Laboratory experiments on rock samples and hydraulic fracturing analysis show that shear failure precedes the occurrence of tensile failure (Amadei and Stephansson 1997). Consequently, we have assumed $P_S < P_T$, even though close. This justifies why the shear and tensile failure front are similar, even if on average the shear front is slightly advanced with respect to the tensile front.

The event cloud can be re-scaled (Hummel and Shapiro 2013). The scaling approach transforms a cloud of seismic events from one medium corresponding to an effective hydraulically homogeneous anisotropic nonlinear one into a microseismic cloud corresponding to an equivalent hydraulically homogeneous isotropic medium. This procedure applied to real data allows the identification of the degree of nonlinearity on the basis of the behavior of the triggering front (Shapiro *et al* 1999). The re-scaled coordinates are given by $x_i = \sqrt{D_0/D_1}\,x_i'$ according to equation (16) and the envelope (64) becomes the circle

$$x_1^2 + x_3^2 = 6D_0 t, \qquad (38)$$

where $D_0 = 1.32 \times 10^{-4}\ \mathrm{m^2\,s^{-1}}$ is used to obtain a good fit. Note that the actual $D_0 = 1.65 \times 10^{-5}\ \mathrm{m^2\,s^{-1}}$, i.e. 8 times lower, and that equation (38) is strictly valid for a linear diffusion equation (pressure-independent permeability). The results for the shear events at 24 and 48 h are shown in figure 10.

Next, we use the $r$–$t$ plot of induced events to obtain the envelope or triggering front in a more accurate way than the preceding 2D fronts. We consider the shear events at 5 and 48 h diffusion times (in order to verify the trend of the front) and use equation (67),

$$r = (at)^b, \qquad (39)$$

to compute the envelopes. The results are shown in figure 11, where the solid and dashed lines correspond to cubic and

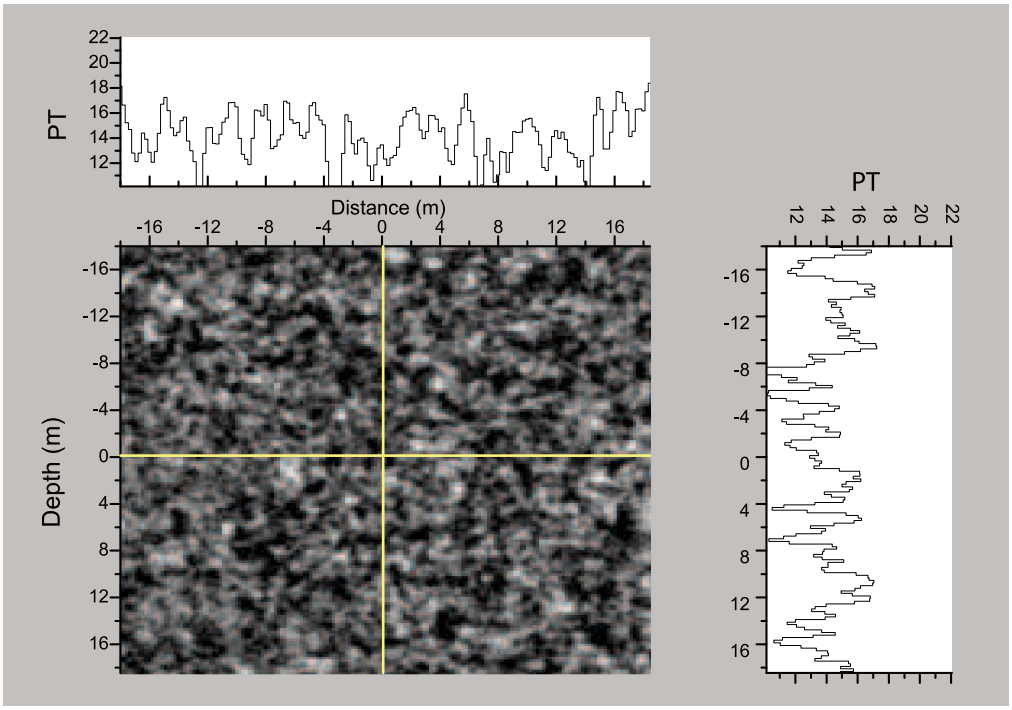


**Figure 7.** Random distribution of the failure criterion $P_T$ (in MPa). The medium is divided into 165 × 165 cells. The fractal parameters are $P_0 = P_T$ ($P_0 = P_S$ in the shear case), with $\Delta P_m = 60\%\ P_0$, $\nu = 0.18$, $l = 0.2$ m and $d = 3$. The top and right plots corresponds to the yellow vertical and horizontal lines. (See Wu (2006) for values of the tensile strength.)

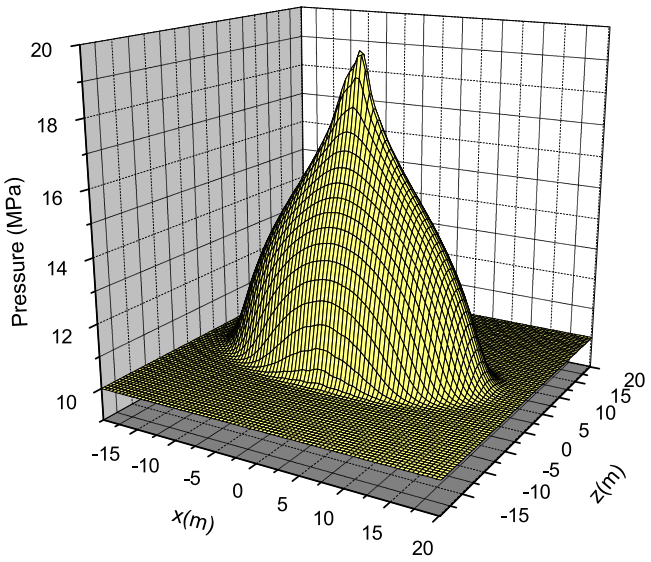


**Figure 8.** Pressure field obtained with Comsol ($p_1 = 1.5$ MPa) for an unbounded homogeneous medium, where the permeability components along the $x$- and $z$-directions are given in table 1. The anisotropic character of the diffusion becomes clear. The field diffuses faster into the formation along the $x$-direction, since the permeability is higher than that of the vertical $z$-direction.

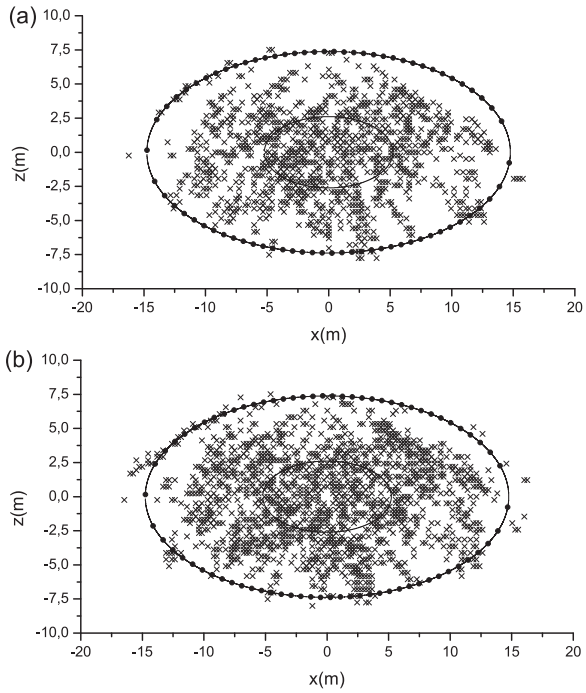


**Figure 9.** Cloud of tensile (a) and shear (b) events after 48 h of fluid injection, where the number of induced events is 2255 and 3081, respectively. The inner front (solid line) is obtained with equation (64), while the outer front is obtained with the same equations but assuming 8 times the diffusivity components $D_1$ and $D_3$.

square root behaviors, i.e. $b = 1/3$ and $b = 1/2$, with $a = 0.01$ m$^3$ s$^{-1}$ and $a = 0.0018$ m$^2$ s$^{-1}$, respectively (a) and $a = 0.013$ m$^3$ s$^{-1}$ and $a = 0.001$ m$^2$ s$^{-1}$, respectively (b). As can be seen, the cubic root triggering front provides a better fit, as it is the case of Barnett shale (Hummel 2013). Hummel and Shapiro (2013) found that the permeability follows a pressure dependence in Barnett shale described by a $p^n$ power law, with $n$ larger than 7, and a $t^{1/3}$ envelope after 5 h of injection (see their figure 1 and compare it to our figure 11(a). However, a better fit at 24 h emission time is obtained with a triggering front of the form $(at)^b$, where $a = 0.008$ m$^{1/0.355}$/s

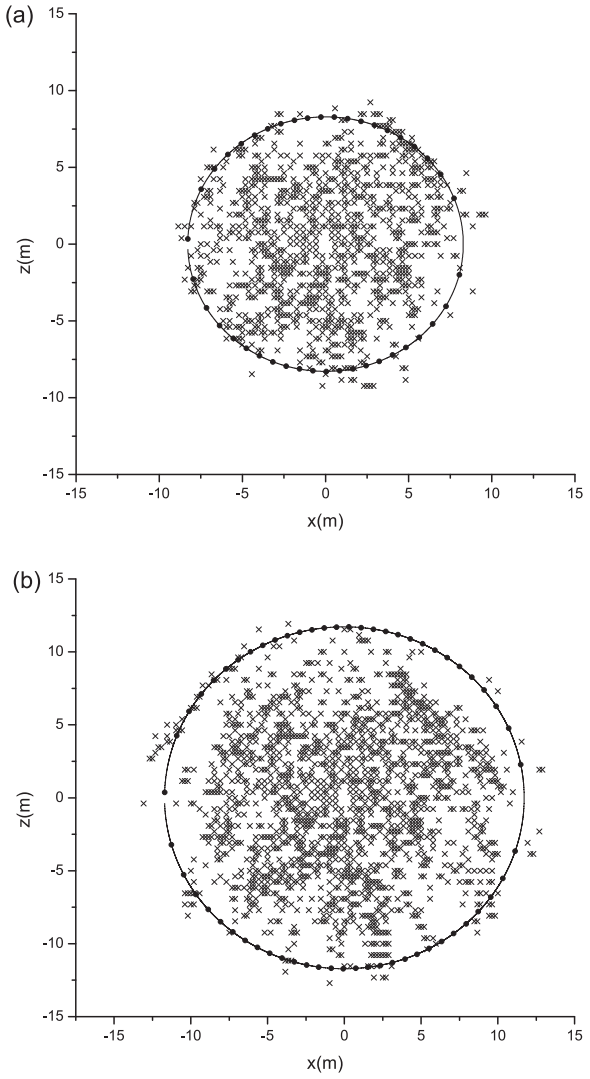


**Figure 10.** Re-scaled events corresponding to the shear events at $t = 24$ h (a) (1959 events) and $t = 48$ h (3081 events) (compare figure 10(b) with figure 9(b). These clouds correspond to an equivalent isotropic medium.

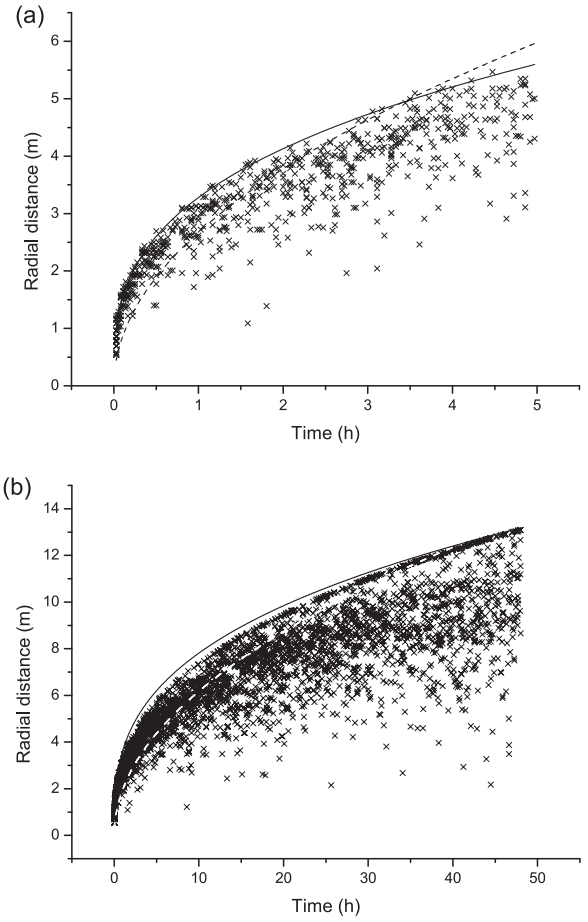


**Figure 11.** Location of the shear events (re-scaled) as a function of the emission time at 5 h (a) and 48 h (b). The solid and dashed lines correspond to a triggering front with a $t^{1/3}$ and $t^{1/2}$ dependences. As can be seen, the cubic root triggering front provides a better fit, as it is the case of Barnett shale (Hummel 2013).

and $b = 0.355$ as can be seen in figure 12, where the events with a maximum time of 24 h are shown. It can be shown that using equation (36) with $p_1 = 1.5$ MPa, the triggering front follows a square root time dependence, indicating the importance of using accurate pressure solution for estimating the front evolution. Although we obtain almost a similar exponent as Hummel and Shapiro (2013) (0.355 against 0.357), we have used an exponential function while the authors consider a $p^7$ dependence.

Hummel and Shapiro (2012) show for an exponential dependence of permeability versus pressure, a square root of time triggering front is obtained. This seems to be the case for relatively high-permeability rocks, such as sandstones. Here, we found that we pass from a square root behavior for sandstones to an almost cubic-root behavior for shales. In addition, we performed tests with a uniform random distribution in the range [10, 20] MPa for the critical pressures and an exponential dependence for the permeability. From

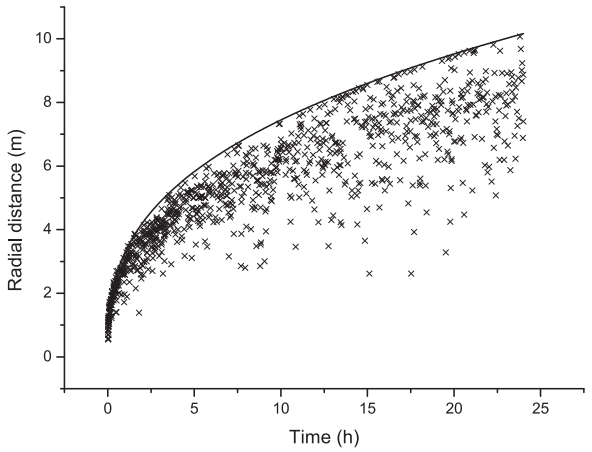


**Figure 12.** Location of the shear events (re-scaled) as a function of the emission time at 24 h. The solid line corresponds to a triggering front of the form $(at)^b$, where $a = 0.008$ m$^{1/0.355}$/s and $b = 0.355$. It can be shown that using equation (36) with $p_1 = 1.5$ MPa, the triggering front follows a square root time dependence, indicating the importance of using accurate pressure solution for estimating the front evolution. Although we obtain almost a similar exponent as Hummel and Shapiro (2013) (0.355 against 0.357), we have used an exponential function while the authors consider a $p^7$ dependence.

these tests, we obtained exponents $b$ decreasing from 0.5 (for sandstones) to 0.4 (for shales), i.e., it depends on the permeability and also on the degree of nonlinearity $p_1$. Clearly, depending on the level of nonlinearity and permeability, the nature of the triggering front changes. Considering an exponential dependence of permeability on pressure as well as a point injection source, the triggering front is characterized by the square root of time behavior (Hummel and Shapiro 2012). Once the point injection source changes into a source of finite extent, this nature changes from a square root into a cubic root of time dependence. However, this change depends on the permeability as well as on the nonlinearity. This is an issue to test in future publications, i.e, the influence of the extent of a finite source on the change of the nature of the triggering front, In summary, if the injection source is a point (or the event is far away from a finite injection cavity), the exponential diffusion should in principle produce a square root, subject to the previous conditions. The finite-source effect may lead to an apparent cubic-root behavior.

It is shown that the triggering front induced by fluid injection contains information about the permeability dependence on pore pressure and the anisotropic properties of the hydraulic diffusivity. These features can univocally be resolved as a function of the injection time and distance from the borehole, as shown by the modeling results. The comparison of synthetic and real data (see figure 5 in Hummel and Shapiro 2013) shows differences in the event distributions. While the synthetic seismicity distribution shows a very sharp triggering front, the real data is characterized by a diffuse boundary. This is explained by the heterogeneity of the real medium, while here we are assuming an equivalent homogenous medium. Moreover, in the modeling, we consider a radially symmetric medium. Therefore, possible radial heterogeneity around the borehole may affect the distribution of events and the triggering front. In spite of these differences in the event distributions, we observe some general agreements as in the case of Barnett shale.

An important issue is the interaction of the induced fractures with natural fracture systems/networks in hydraulic fracturing processes. The planar nature of the induced fractures may become 3D, since the orientation of the (re-)activated fractures is generally perpendicular to the main hydraulic fracture orientation. The presence of these re-activated natural fractures explains the anisotropic 3D character of the triggering front. Together, natural and induced fractures form a complex fracture network whose interaction may affect the event cloud (Gale *et al* 2007).

Another aspect of hydraulic fracturing considers the type fluid being injected. Hydraulic fracturing treatments across the various unconventional shale plays around the globe are seldom carried out considering pure brine as a treatment fluid. More than often, additives (proppants) are used for numerous purposes and reasons and special care needs to be applied when handling such treatment fluids. This issue is in some way a 'limitation' of the modeling conducted in this work. Generally, the pressure decreases after the injection and the increasing effective normal stress stabilizes the rock, closing the induced cracks and fractures. This can be prevented by the use of proppants, leading to a post-injection enhanced hydraulic permeability. To model this situation, Hummel and Shapiro (2016) and Johann *et al* (2016) introduced the concept of 'frozen diffusivity' and implemented numerical models considering a different behavior of the hydraulic diffusivity after the injection stop, since the microseismic activity continues after the termination of the injection. Nonlinearity is also reflected in the post-injection regime. However, this, goes beyond the scope of this paper and requires further analysis/investigation.

The amplitude of a microseismic event is proportional to its seismic moment. The size of the event cloud can be related to the seismic moment as $M_0 = \mu_m S d$, where $S$ is the fracture area and $d$ is the displacement. Magnitudes (or rupture scale) can be included statistically to a given triggered hypocenter. Shapiro *et al* (2011) approximated a stimulated volume by an ellipsoid and compared the statistics of induced events with that of randomly distributed thin flat disks modeling rupture surfaces. They quantified the impact of the geometry of that volume on the Gutenberg–Richter-type frequency-magnitude distribution, showing that monitoring the spatial growth of seismicity in real time can help to constrain the risk of inducing damaging earthquakes. In another paper Shapiro *et al* (2013) have derived lower and upper bounds of the probability to induce a given-magnitude event. The bounds depend on the minimum principal axis of the stimulated volume. The observed frequency-magnitude curves seem to follow mainly the lower bound, with exceptions of some large-magnitude events clearly deviating from this statistic. However, regarding magnitudes, it would be an important step towards further understanding of induced event physics. Yet, determination of magnitudes is beyond the scope of the work presented here and should be considered as an issue for future works.

## 5. Conclusions

Shale gas extraction requires that a treatment fluid is injected at high flow rates to enhance permeable flow paths around the borehole. This process, which increases the medium permeability, is described by a nonlinear diffusion equation, i.e. the permeability and the hydraulic diffusivity depend on pressure. We have solved this equation and establish fracture criteria to model the emission of tensile and shear events caused by the injection. Snapshots and $r$–$t$ plots are particularly useful to characterize the fracturing and obtain information of the medium properties. The model considers anisotropic permeability and the results are spatially re-scaled to obtain an effective isotropic medium.

We considered two typical cases of fluid injection. First, Wu and Pruess's solution for a constant mass flow in cylindrical coordinates and second Yeung *et al*'s solution for a constant injection pressure in spherical coordinates, generalizing both approaches to the anisotropic case. The first solution only hold for high permeabilities and the second solution can be used for shales but for moderate pressure dependence of the permeability.

For a 3D fluid diffusion in spherical coordinates and a strong exponential pressure dependence, we have used numerical solutions provided by the Comsol software. The $r$–$t$ curves in the re-scaled domain reveal a $t^{1/3}$ signature (as already observed in Barnett shale). Use of the classical front (permeability pressure independent, $\sqrt{t}$ signature) to fit cloud events spatially, provides good results but with a re-scaled value of the (initial) permeability components. Modeling is required to evaluate the scaling constant, which in the example presented here is close to eight for all diffusion times.

In summary, the location of the events in depth can then be used to obtain the diffusivity and the permeability if the stiffness of the formation is known, for instance, from seismic or sonic data. Moreover, the event cloud yields the anisotropy of the medium and its evolution during the injection. Modeling is required to quantify the extension of the cloud along the three spatial dimensions. In the example we have considered an exponential pressure dependence of permeability but the approach can be applied to other functions such as power laws.

## Appendix A. Solution of the pressure equation in cylindrical coordinates and constant mass injection

The solution presented here is an integral solution for a 1D radial flow and considers the fluid injection in an infinite horizontal reservoir of constant thickness, and the formation is saturated with a single fluid. The solution, which can be found in Wu and Pruess (2000) has been originally tested against the numerical code MULKOM-GWF. These authors claim that the solutions provide a good approximate solution to a general nonlinear governing flow equation with arbitrary constitutive correlations of permeability, porosity and fluid density as functions of pore pressure.

We solve equation (11) subject to the initial condition

$$p(r,\,0) = p_{\rm i} \tag{40}$$

and boundary condition

$$-\frac{2\pi r_0 h}{\eta}[\rho(p)\kappa(p)\partial_r p]_{r=r_0} = Q, \tag{41}$$

where $\kappa = \bar{\kappa} f(p)$, $Q$ is the mass injection rate, $r_0$ is the borehole radius and $h$ is the thickness of the formation. We recall here that $r$ is actually $r'$ as given in equation (12) because we have omitted the primes for simplicity.

We consider the case when the compressibility is small and pressure independent and the fluid density is a linear function of pressure (Wu and Pruess 2000). In this case the solution is

$$\begin{aligned} p(r,\,t) &= p_{\rm i} - \frac{\eta Q}{2\pi h\rho(p_0)\kappa(p_0)}\left(1+\frac{1}{2\beta}\right)\ln \\ &\times\left[\frac{2(r/r_0)}{1+\beta} - \left(\frac{r/r_0}{1+\beta}\right)^2\right], \quad r_0 \leqslant r \leqslant r_0 + d(t), \\ p(r,\,t) &= p_{\rm i}, \quad r > r_0 + d(t) \end{aligned} \tag{42}$$

where $p_0(t)$ and $d(t)$ are the borehole pressure and penetration distance, respectively, with $\beta = d/r_0$ (Wu and Pruess 2000 equation (28)).

An additional equation can be obtained from the mass balance equation,

$$\begin{aligned} &t + \frac{r_0^2\rho_{\rm i}\phi C\eta}{\rho(p_0)\kappa(p_0)}\left(\frac{1+2\beta}{2\beta}\right) \\ &\times\left[-\beta\left(2 + \frac{3}{2}\beta\right) + 2(1+\beta)^2\ln(1+\beta)\right. \\ &\left. - \frac{1}{2}[1-4(1+\beta)^2]\ln\left[\frac{1+2\beta}{(1+\beta)^2}\right]\right] = 0 \end{aligned} \tag{43}$$

(Wu and Pruess 2000 equation (31)). The solution $p$ is obtained by solving simultaneously equations (42) and (43) at $r = r_0$ for $p_0(t)$ and $\beta(t)$ and then substituting these values into (42). Another solution developed by Wu and Pruess (2000) (not reported here) is given by their set set of equations (25), (30), which provides less accuracy as shown in the results (section 4).

The assumed constitutive equations are

$$\rho(p) = \rho_{\rm i} + \upsilon(p - p_{\rm i}),\ \kappa(p) = \bar{\kappa} f(p), \tag{44}$$

where $\rho_{\rm i}$ and $\upsilon$ are constants ($\upsilon = 0$ in this work). Porosity and density are assumed to be constant, since its variations can be neglected. Permeability changes are mainly due to opening of cracks, i.e. compliant porosity is negligible.

The exact solution of equation (11) when there is no pressure dependence is

$$p(r,\,t) = p_{\rm i} + \frac{Q\eta}{4\pi\rho\bar{\kappa}h}E_1\left(\frac{\phi\eta C r'^2}{4\bar{\kappa}t}\right) \tag{45}$$

(Wu and Pruess 2000 equation (38)), where $E_1(x) = -E{\rm i}(-x)$ is an exponential integral, $\bar{\kappa}$ is given in equation (9) and $r'$ in equation (12).

## Appendix B. Solution of the pressure equation in spherical coordinates and constant pressure injection

The equations obtained in this appendix are based on Yeung *et al*'s (1993) approximate solutions to the diffusive problem with pressure-dependent permeability, assuming a constant pressure injection regime in an infinitely large porous medium.

Substituting equation (22) into the pressure equation (21) we obtain

$$\frac{1}{p_1}(\partial_r p)^2 + \frac{2}{r}\partial_r p + \partial_{rr}^2 p = \frac{1}{D_0}\dot{p}\exp[-(p-p_{\rm i})/p_1]. \tag{46}$$

Let us define the dimensionless variables

$$\hat{p} = \frac{p_{\rm i} - p}{p_{\rm i} - p_0},\quad \hat{t} = \frac{D_0 t}{r_0'^2},\quad \hat{r} = \frac{r}{r_0'},\quad \hat{p}_1 = \frac{p_1}{p_{\rm i} - p_0}, \tag{47}$$

where

$$r_0' = \sqrt{\frac{D_0}{D_1}(x_0^2 + y_0^2) + \frac{D_0}{D_3}z_0^2}, \tag{48}$$

where $(x_0, y_0, z_0)$ correspond to the radial distance $r_0$, and here, for clarity, we have used the notation $(x_1, x_2, x_3) = (x, y, z)$. Then, equation (46) becomes

$$-\frac{1}{\hat{p}_1}\left(\frac{\partial \hat{p}}{\partial \hat{r}}\right)^2 + \frac{2}{\hat{r}}\frac{\partial \hat{p}}{\partial \hat{r}} + \frac{\partial^2 \hat{p}}{\partial \hat{r}^2} = \frac{\partial \hat{p}}{\partial \hat{t}}\exp[\hat{p}\ /\hat{p}_1]. \tag{49}$$

Let us define the transformed variable

$$q = \hat{p}_1[1 - \exp(-\hat{p}/\hat{p}_1)], \tag{50}$$

such that

$$\hat{p} = -\hat{p}_1 \ln\left(1 - \frac{q}{\hat{p}_1}\right). \tag{51}$$

Equation (49) reduces to

$$\frac{2}{\hat{r}}\frac{\partial q}{\partial \hat{r}} + \frac{\partial^2 q}{\partial \hat{r}^2} = \left(1 - \frac{q}{\hat{p}_1}\right)^{-1}\frac{\partial q}{\partial \hat{t}}. \tag{52}$$

In the limit $\hat{p}_1 \to \infty$, we have $q = \hat{p}$ and we obtain the classical diffusion equation.

Pedrosa (1986) and Kikani and Pedrosa (1991) obtained an approximate solution of the spherical flow problem and Yeung *et al* (1993) use this approximation to solve equation (52) by expanding $q$ in terms of $\hat{p}_1$. They show that for a given range of values of this parameter, the following zero-order term solution is accurate enough:

$$\frac{2}{\hat{r}}\frac{\partial q_0}{\partial \hat{r}} + \frac{\partial^2 q_0}{\partial \hat{r}^2} = \frac{\partial q_0}{\partial \hat{t}} \tag{53}$$

(Yeung *et al* 1993 equation (20)). We can verify that this equation is a consequence of the approximation $q/\hat{p}_1 \ll 1$ in equation (52). According to (50) this means $1 - [1 - \exp(-\hat{p}/\hat{p}_1)] \approx 1$ or $1 - [1 - \exp[(p - p_i)/p_1)] \approx 1$. Thus, the solution is accurate for values of $r$ satisfying this condition.

Equation (53) is similar to the constant diffusivity equation. The solution is

$$q_0 = \frac{\hat{p}_1}{\hat{r}}[1 - \exp(-1/\hat{p}_1)]\operatorname{erfc}\left(\frac{\hat{r} - 1}{2\sqrt{\hat{t}}}\right) \tag{54}$$

(Carslaw and Jaeger 1959) and, consequently,

$$\hat{p} = -\hat{p}_1 \ln\left[1 - \frac{[1 - \exp(-1/\hat{p}_1)]}{\hat{r}}\operatorname{erfc}\left(\frac{\hat{r} - 1}{2\sqrt{\hat{t}}}\right)\right], \tag{55}$$

where erfc is the complementary error function. If the diffusivity is constant ($\hat{p}_1 \to \infty$), we obtain the classical solution

$$\hat{p} = \frac{1}{\hat{r}}\operatorname{erfc}\left(\frac{\hat{r} - 1}{2\sqrt{\hat{t}}}\right). \tag{56}$$

Let us obtain now the volumetric injection rate at $r_0$ corresponding to the constant pressure injection. The definition is

$$Q = -4\pi r_0^2 \frac{\kappa_1}{\eta}\frac{\partial p}{\partial r}\bigg|_{r=r_0}$$
$$= -4\pi r_0^2 \frac{D_1}{N}\exp[(p - p_i)/p_1]\frac{\partial p}{\partial r}\bigg|_{r=r_0}, \tag{57}$$

where $4\pi r_0^2$ is the surface of the cavity of radius $r_0$ and we have considered the horizontal plane. In terms of dimensionless quantities we have

$$Q = \frac{4\pi r_0^2 D_1(p_i - p_0)}{r_0' N}\hat{Q}, \tag{58}$$

where

$$\hat{Q} = -\exp(-\hat{p}\ /\hat{p}_1)\frac{\partial \hat{p}}{\partial \hat{r}}\bigg|_{\hat{r}=1} \tag{59}$$

is the dimensionless flux. We obtain from equation (59),

$$\hat{Q} = \hat{p}_1[1 - \exp(-1\ /\hat{p}_1)]\left[1 + \frac{1}{\sqrt{\pi \hat{t}}}\right] \tag{60}$$

(Yeung *et al* 1993 equation (27)).

## Appendix C. Triggering front

An approximation to the triggering front can be obtained when the properties are constant and the diffusivity is pressure independent. Equation (17), with an external point source, can be expressed as

$$\dot{p} = D_0 \Delta' p + \delta(t)\delta(\mathbf{r}' - \mathbf{r}_0'), \tag{61}$$

where $\mathbf{r}_0'$ is the source location and $\delta$ is Dirac's delta. The solution is the Green function

$$g(\mathbf{r}', \mathbf{r}_0', t) = \frac{1}{(4\pi D_0 t)^{\xi/2}}\exp[-|\mathbf{r}' - \mathbf{r}_0'|^2/(4D_0 t)], \tag{62}$$

where $\xi$ is the space dimension (Carslaw and Jaeger 1959, Carcione 2014).

The maximum of the function $g(t)$ is located at

$$t = \frac{|\mathbf{r}' - \mathbf{r}_0'|^2}{2\xi D_0}. \tag{63}$$

In the physical 3D space, combining equations (19) and (63), we obtain

$$\frac{|\mathbf{r}' - \mathbf{r}_0'|}{\sqrt{D_0}} \approx \sqrt{\frac{x_1^2 + x_2^2}{D_1} + \frac{x_3^2}{D_3}} = \sqrt{2t\xi} = \sqrt{6t}, \tag{64}$$

indicating that the front is anisotropic, i.e. the front arrives at time $t = (x_1^2 + x_2^2)/(6D_1)$ at a receiver located at distance $\sqrt{x_1^2 + x_2^2}$ from the source and at time $t = x_3^2/(6D_3)$ at a receiver located at distance $x_3$ from the source. Equivalently, if the distances are the same, say $r$, the front employs $t_1 = r^2/(6D_1)$ along the horizontal direction and $t_3 = r^2/(6D_3)$ along the $z$-direction to travel the distance $r$.

Equation (64) represents an ellipse. The previous reasoning is an attempt of defining the triggering front on the basis of the Green function, but actually, the triggering front is a heuristic quantity defining a beginning of a more-or-less significant relaxation. It is 'the distance traveled in time $t$ by the phase front of a harmonic pore pressure diffusion wave of frequency $2\pi/t$' (see p 128 in Shapiro 2015). For a given diffusivity $D$, it is $\sqrt{4\pi Dt}$ and indeed proportional to $\sqrt{6Dt}$.

In the nonlinear case, i.e. when the diffusivity is pressure-dependent, the triggering front differs substantially from equation (64). Shapiro and Dinske (2009) and Hummel and Shapiro (2013) find that for a constant flow rate of injection $Q$ and a power law diffusivity dependence of the form (25) the triggering front is

$$r \propto (D_0 Q^n t^{n+1})^{1/(3n+2)}, \tag{65}$$

which for $n \gg 1$ yields

$$r \propto (Qt)^{1/3}. \tag{66}$$

However, in real situations they have used the following equation:

$$r = (at)^b, \tag{67}$$

along a given direction, where $a$ and $b$ are constants.

## Appendix D. Fractal failure criterion

We vary the threshold $P$ fractally. Let $\Delta P_m$ be the maximum deviation from the background value $P_0$. $P$ at $r$ is first subjected to the variations $(\Delta P)^r$, such that

$$-\Delta P_m \leqslant (\Delta P)^r \leqslant \Delta P_m, \tag{68}$$

where $(\Delta P)^r$ is obtained from a random generator, and the superindex '$r$' denotes random. (Random numbers between 0 and 1 are generated and then scaled to the interval $[-1, 1]\Delta P_m$).

The fractal variations can be described by the von Kármán autocovariance function. The exponential function used by Rothert and Shapiro (2003) is a particular case of this function, which is widely used in seismic applications (e.g., Carcione *et al* 2003). The corresponding wavenumber-domain power spectrum of the von Kármán function is

$$S(k_1, k_2, k_3) = C(1 + k^2 l^2)^{-(\nu+d/2)}, \tag{69}$$

where $k = \sqrt{k_1^2 + k_2^2 + k_3^2}$ is the wavenumber, $l$ is the correlation length, $\nu$ $(0 < \nu < 1)$ is a self-similarity coefficient, $C$ is a normalization constant, and $d$ is the Euclidean dimension. The von Kármán correlation function describes self-affine, fractal processes of fractal dimension $d + 1 - \nu$ at scales smaller than $l$.

The threshold $P$ is then calculated as

$$P(x, y, z) = P_0 \pm \Delta P(x, y, z), \tag{70}$$

where

$$\widetilde{\Delta P}(k_1, k_2, k_3) = \widetilde{(\Delta P)}^r(k_1, k_2, k_3) S(k_1, k_2, k_3), \tag{71}$$

with $\widetilde{(\Delta P)}^r(k_1, k_2, k_3)$ being the Fourier transform of $(\Delta P)^r(x, y, z)$. The tilde denotes the space Fourier transform.

## ORCID iDs

José M Carcione https://orcid.org/0000-0002-2839-705X
Gilda Currenti https://orcid.org/0000-0001-8650-5613
Lisa Johann https://orcid.org/0000-0003-3513-1943
Serge Shapiro https://orcid.org/0000-0002-5062-2698

## References

Amadei B and Stephansson O 1997 *Rock Stress and its Measurement* (London: Chapman and Hall)
Best M E and Katsube T J 1995 Shale permeability and its significance in hydrocarbon exploration *Leading Edge* **14** 165–70
Carcione J M 2014 *Wave Fields in Real Media. Theory and Numerical Simulation of Wave Propagation in Anisotropic, Anelastic, Porous and Electromagnetic Media* 3rd edn (Amsterdam: Elsevier)
Carcione J M, Da Col F, Currenti G and Cantucci B 2015 Modeling techniques to study $CO_2$-injection induced micro-seismicity *Int. J. Greenhouse Gas Control* **42** 246–57
Carcione J M, Finetti I and Gei D 2003 Seismic modeling study of the Earth's deep crust *Geophysics* **68** 656–64
Carcione J M and Gei D 2009 Theory and numerical simulation of fluid-pressure diffusion in anisotropic porous media *Geophysics* **74** N31–9
Carcione J M, Helle H B and Gangi A F 2006 Theory of borehole stability when drilling through salt formations *Geophysics* **71** F31–47
Carcione J M and Poletto F 2013 Seismic rheological model and reflection coefficients of the brittle-ductile transition *Pure Appl. Geophys.* (https://doi.org/10.1007/s00024-013-0643-4)
Carslaw H S and Jaeger J C 1959 *Conduction of Heat in Solids* (Oxford: Clarendon)
Colmenares L B and Zoback M D 2002 A statistical evaluation of intact rock failure criteria constrained by polyaxial test data for five different rocks *Int. J. Rock Mech. Min.* **39** 695–729
Comsol Multiphysics 2014 *Reference Manual 5.0, Comsol Ab* (Stockholm) 1262 pp
David C, Wong T-F, Zhu W and Zhang J 1994 Laboratory measurement of compaction-induced permeability change in porous rocks: implications for the generation and maintenance of pore pressure excess in the crust *Pure Appl. Geophys.* **143** 425–56
Engelder T 1993 *Stress Regimes in the Lithosphere* (Princeton, NJ: Princeton University Press)
Gale J F W, Reed R M and Holder J 2007 Natural fractures in the Barnett shale and their importance for hydraulic fracture treatments *AAPG Bull.* **91** 603–22
Gangi A F 1978 Variation of whole and fractured porous rock permeability with confining pressure *Int. J. Rock Mech. Min. Sci. Geomech. Abstr.* **15** 249–57
Gangi A F 1981 The variation of mechanical and transport properties of cracked rock with pressure *Proc. US Symp. on Rock Mechanics* vol 22, pp 85–9
Gangi A F and Carlson R L 1996 An asperity-deformation model for effective pressure *Tectonophysics* **256** 241–51
Gutierrez M S and Lewis R W 2002 Coupling of fluid flow and deformation in underground formations *J. Eng. Mech.* **128** 779–87

Hummel N 2013 Pressure-dependent hydraulic transport as a model for fluid induced earthquakes *PhD Thesis* Freie Universität Berlin

Hummel N and Müller T M 2009 Microseismic signatures of non-linear pore-fluid pressure diffusion *Geophys. J. Int.* **179** 1558–65

Hummel N and Shapiro S A 2012 Microseismic estimates of hydraulic diffusivity in case of non-linear fluid-rock interaction *Geophys. J. Int.* **188** 1441–53

Hummel N and Shapiro S A 2013 Nonlinear diffusion-based interpretation of induced microseismicity: a Barnett shale hydraulic fracturing case study *Geophysics* **78** B211–26

Hummel N and Shapiro S A 2016 Back front of seismicity induced by non-linear pore pressure diffusion *Geophys. Prospect.* **64** 170–91

Johann L, Dinske C and Shapiro S A 2016 Scaling of seismicity induced by nonlinear fluid-rock interaction after an injection stop *J. Geophys. Res. Solid Earth* **121** 8154–74

Kikani J and Pedrosa O A Jr 1991 Perturbation analysis of stress-sensitive reservoirs *SPE Form. Eval.* **6** 379–86

Lal M 1999 Shale stability: drilling fluid interaction and shale strength *SPE Asia Pacific Oil and Gas Conference and Exhibition* 54356-MS

Langenbruch C and Shapiro S A 2015 Quantitative analysis of rock stress heterogeneity: implications for the seismogenesis of fluid-injection-induced seismicity *Geophysics* **80** WC73–88

Langenbruch C and Shapiro S A 2014 Gutenberg–Richter relation originates from Coulomb stress fluctuations caused by elastic rock heterogeneity *J. Geophys. Res. Solid Earth* **119** 1220–34

Louis C 1974 Rock hydraulics *Rock Mechanics* ed L Müller (New York: Springer) pp 300–87

Palmer I D and Mansoori J 1998 How permeability depends upon stress and pore pressure in coalbeds: a new model *SPE Reservoir Eval. Eng.* **1** 539–43

Pedrosa O A Jr 1986 Pressure transient response in stress-sensitive formations *SPE California Regional Meeting (Oakland, CA 2–4 April)*

Rothert E and Shapiro S A 2003 Microseismic monitoring of borehole fluid injections: data modelling and inversion for hydraulic properties of rocks *Geophysics* **68** 685–9

Rothert E and Shapiro S A 2007 Statistics of fracture strength and fluid- induced microseismicity *J. Geophys. Res.* **112** B04309

Rutqvist J, Rinaldi A P, Cappa F and Moridis G J 2015 Modeling of fault activation and seismicity by injection directly into a fault zone associated with hydraulic fracturing of shale-gas reservoirs *J. Pet. Sci. Eng.* **127** 377–86

Shapiro S A 2015 *Fluid-Induced Seismicity* (Cambridge: Cambridge University Press)

Shapiro S A, Audigane P and Royer J J 1999 Large-scale *in situ* permeability tensor of rocks from induced microseismicity *Geophys. J. Int.* **137** 207–13

Shapiro S A and Dinske C 2009 Scaling of seismicity induced by nonlinear fluid-rock interaction *J. Geophys. Res. Solid Earth* **114** B09307

Shapiro S, Krüger O S and Dinske C 2013 Probability of inducing given-magnitude earthquakes by perturbing finite volumes of rocks *J. Geophys. Res. Solid Earth* **118** 3557–75

Shapiro S, Krüger O S, Dinske C and Langenbruch C 2011 Magnitudes of induced earthquakes and geometric scales of fluid-stimulated rock volumes *Geophysics* **76** WC53–61

Shi J-Q and Durucan S 2016 Near-exponential relationship between effective stress and permeability of porous rock revealed in Gangi's phenomenological models and application to gas shales: *Int. J. Coal Geol.* **154** 111–22

Wu R 2006 Some fundamental mechanisms of hydraulic fracturing *PhD Thesis* Georgia Institute of Technology

Wu Y S and Pruess K 2000 Integral solutions for transient fluid flow through a porous medium with pressure-dependent permeability *Int. J. Rock Mech. Min. Sci.* **37** 51–61

Yeung K, Chakrabarty C and Zhang X 1993 Approximate analytical study of aquifers with pressure-sensitivity formation permeability *Water Resour. Res.* **29** 3495–501